Deep learning assisted processing of synchrotron-based micro-CT imaging of fast, dynamic multiphase flow in porous media

Eric Sonny **Mathew**[1], *Michael* **Camilleri**[2], *Quan* **Zheng**[3], *Yufu* **Niu**[4], *Bianca* **Brandstätter**[5], *Kunning* **Tang**[3], *Peyman* **Mostaghimi**[1], *Ryan T.* **Armstrong**[1], *Samuel* **Jackson**[2]

[1]School of Civil and Environmental Engineering, University of New South Wales, Sydney, Australia
[2]CSIRO Energy, Clayton South, Australia
[3]School of Minerals and Energy Resources Engineering, University of New South Wales, Sydney, Australia
[4]CSIRO Mineral Resources, Lucas Heights, Australia
[5]Department Geoenergy, University of Leoben, Leoben, Austria

Abstract. The Australian Synchrotron micro-CT beamline was used to capture fast multiphase flow scans at 1s with 15-16s time lapse intervals at 3.6µm resolution. Two phase drainage flow experiments were conducted using a custom-built rig with a water-wet and a mixed-wet Bentheimer sandstone sample to observe the percolation of fluids in the pore spaces. During each injection cycle, fast dynamic batches of 50 scans were taken resulting in large volumes of data. Conventional methods of image processing would not only be time consuming but could also lead to misclassification of phases, especially due to the presence of streak artifacts in the datasets. A workflow was established using the Sci-Py library for data preprocessing (translation and rotation) of fast batch scans followed by a U-ResNet model for the accurate segmentation of the images. 25000 2D paired gray-scale and WEKA segmented 256x256 pixel patches were used for training the model, the mean Intersection-Over-Union (mIoU) showed an accuracy of 0.93 during the testing phase. While phase accuracy on unseen dataset was recorded on an average as 0.93, and mIoU of 0.96, visual examination indicated that streak artifacts had been minimized. U-ResNet model was further compared with watershed-based segmentation in terms of accuracy, speed and 2D Minkowski functionals.

1 Introduction

The study of two-phase flow in porous media is essential to address several geological challenges like the environmental remediation of aquifers, hydrocarbon recovery, and carbon dioxide sequestration in geological reservoirs [1-3]. In the field of digital rock physics (DRP), an important tool for such studies of pore-scale flow is microcomputed tomography (micro-CT), which is a non-destructive imaging tool that captures two-dimensional (2D) trans-axial projections or slices of a target specimen, that can be combined to produce a high resolution three-dimensional (3D) image [4, 5].

With micro-CT, it is critical that the target object does not change substantially during the scanning period, and therefore the flooding is stopped at different fractional flows during the experiment, and imaging is done only at equilibrium or quasi equilibrium [6]. Moreover, due to the low flux of lab-based micro-CT, the acquisition time is restricted to a range of several minutes to a few hours to acquire a high-quality image. This poses as a major challenge as several dynamic pore filling events occur in seconds and sometimes even in sub-second timeframes [6-8]. A low acquisition time in the order of seconds from a micro-CT often result in noisy images that interferes with the interpretation of the data. However, with the advancements in synchrotron based micro-CT systems, this challenge of acquiring fast, dynamic scans with X-ray micro-CT have become possible. This is mainly because the synchrotron radiations that is produced using bending magnets have a flux that is million times brighter than that of laboratory-based micro-CT systems [9]. Berg et al. [7] demonstrated the capture of pore-scale events such as Haines jump [10] and snap-off [11] in real-time using synchrotron based micro-CT systems. This was followed by several studies using synchrotrons to classify similar dynamic pore filling events in real-time [6, 8, 12-17].

A synchrotron based micro-CT is more advanced and has several advantages over laboratory based / polychromatic micro-CT systems, but all X-ray based imagery is associated with some level of noise and artifacts. The two main artifacts commonly seen in scans acquired from synchrotron based micro-CT systems are ring artifacts, and streak artifacts. Ring artifacts are concentric rings that appear in the reconstructed image due to defects in the detectors of the micro-CT resulting in low or high beam intensities. On the other hand, scattered X-rays hitting the detector directly can cause bright pixels in regions resulting in streak artifacts [18]. While ring artifacts can be mitigated using correction algorithms in the reconstruction stage, the streak artifact is a challenge to deal with in the reconstructed images as it interferes with the image classification / segmentation process.

Image segmentation is a method of labelling the voxels in an image into different classes which is later used for computation of several petrophysical properties. Some of the conventional methods for image segmentation are global multi-Otsu thresholding [19], marker-controlled Watershed [20], and converging active contours. Among these methods, most of them require manual inputs and quality control [21]. Hence, it has been found that during the segmentation of an image, both the user bias associated with different methods and the

* Corresponding author: e.mathew@unsw.edu.au

presence of artifacts affect subsequent calculations and pore-scale modelling [22, 23].

Another challenging aspect for synchrotron based micro-CT systems is that a high temporal and spatial resolution needs to be used to effectively capture pore filling events dynamically, which result in more image acquisition during the experiment. This implies that terabytes of reconstructed images need to be processed, and so it can be a tedious and limiting task to utilize standard image processing techniques [24]. Therefore, a more efficient and automatic workflow is a requirement to not only process such large volumes of datasets but also address any related artifacts occurring in the reconstructed images.

With recent advancements in artificial intelligence (AI), deep learning which is a subset of AI is a potential breakthrough in the field of image processing. Deep learning techniques are finding more and more uses in data-driven and image based tasks mainly due to its support from improvements in GPU computing, optimization methods, and neural network architectures. [23]. Within deep learning, some of the common architectures used for pore scale image processing and workflows are Artificial Neural Networks (ANN), Convolutional Neural Networks (CNN), and Generative Adversarial Network (GAN) [23]. Among these different architectures, several studies have performed micro-CT image segmentation using CNN [25-28]. A CNN network comprises of a stack of convolutional layers with activation functions and pooling / down-sampling layers that assist in identifying edges, textures and shapes of an input image. This ability of a CNN network enables multiphase segmentation of an image without any user bias or manual intervention that is commonly associated with traditional image segmentation techniques [25].

The aim herein is to develop a workflow that can assist in processing and segmenting large datasets on the scale of several terabytes. In the first part of the study, data preprocessing such as image translation, and rotation is done using the Python's SciPy [29] library, followed by a confirmation of image registration using Avizo™. In the second part of the study, we propose the use of a U-ResNet [30] model for image segmentation. The performance of this workflow was assessed on fast 1s multiphase flow scans that were conducted on both water-wet and mixed-wet Bentheimer sandstone samples at the Australian Synchrotron micro-CT beamline. The segmentation results from the U-ResNet model were evaluated by not only visually inspecting regions with streak artifacts, but also by using accuracy metrics such as phase accuracy, and mean Intersection-Over-Union (mIoU). Additionally, the two-phase segmentation was further compared with traditional segmentation techniques like watershed in terms of accuracy, speed and 2D Minkowski functionals as a benchmark reference. Overall, this study evaluates the use of deep learning for an efficient, quick and a robust workflow for image processing of large datasets of micro-CT images with minimal user bias.

2 Materials and Methods

In the following subsections, we will discuss the datasets used, the architecture of the U-ResNet model, training protocol of the model, the workflow for image analysis, accuracy and morphological measurements, and finally the comparison of U-ResNet segmented images with traditional segmentation methods like watershed.

2.1. Dataset

Two Bentheimer sandstone (20mm length, 6mm diameter) samples were scanned dynamically during a two-phase coreflooding experiment at the Australian Synchrotron micro-CT beamline located in Clayton, Australia. While one of the samples was initially saturated with brine and classified as water-wet, the 2nd sample was aged for 14 days in crude oil at a temperature of 80 degree Celsius. This controlled ageing process increased the wettability of the sample and so was classified as a mixed-wet sample.

The experimental setup for the coreflooding experiment is depicted in Figure 1 which was custom designed and built to adhere to the facilities available at the Australian Synchrotron micro-CT beamline.

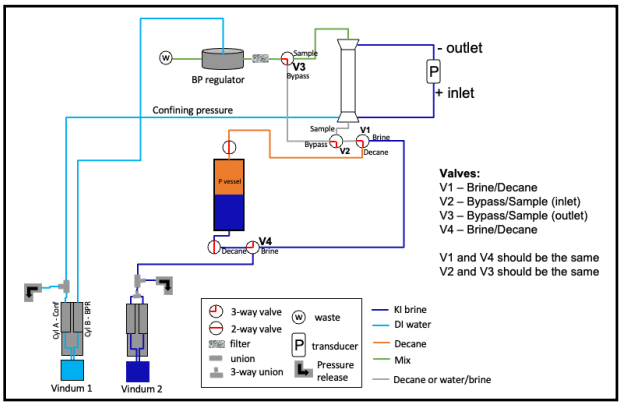

Fig. 1. Experimental setup for two-phase coreflooding experiment custom designed for the Australian Synchrotron micro-CT beamline.

As mentioned earlier, the water-wet sample was first saturated with brine which contained 15% potassium iodide (KI) as a dopant to increase the contrast of phases. Later decane was pumped at 0.03cc/min and the sample was dynamically scanned to capture the percolation of decane through the pore spaces. During this drainage cycle, a fast batch scans consisting of 50 scans were collected at an exposure time of 0.001s with 1001 projections. The core holder was mounted on the rotating stage while the pumps were situated on a custom-built trolley adjacent to the micro-CT table. Due to the flow lines connected to the coreholder, there was a restriction in rotating the sample 360 degrees.

Effectively, the scanning would occur only during the run up to 180-degree rotation phase whereas no scanning would occur when the rotating stage returned to the initial 0-degree position. In this manner a drainage cycle was conducted on the water-wet sample whereby we captured fast multiphase flow scans at 1s with 15-16s time lapse intervals. The scan setting for our experiment was

23.5keV with a magnification of 1.806 to give us scans of 3.6µm resolution. A similar workflow was applied to the mixed-wet sample, and we ran fast batch scans for drainage cycle. Figure 2 depicts slice 0 of (a) fast batch scan number 30 from the 1st drainage cycle of the water-wet sample, and (b) fast batch scan number 18 from the 1st drainage cycle of the mixed-wet sample that was captured during the two-phase flow experiment. The reconstructed images were 16-bit images which were normalized to 8-bit images and then cropped to an image size of 1536 x 1536 x 160 voxels before conducting further image processing and analysis. It is noteworthy to mention that in this paper, drainage cycle refers to decane replacing brine for both water-wet and mixed-wet sample.

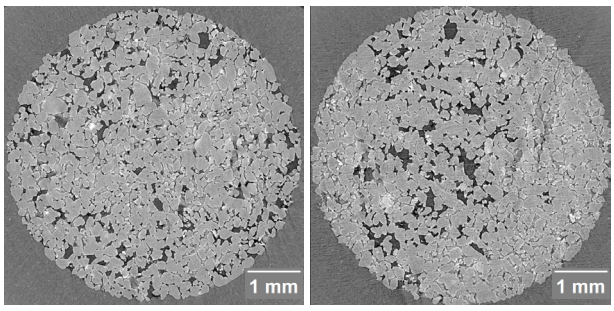

(a) (b)

Fig. 2. Fast batch scan (a) number 30 of the water-wet sample and (b) number 18 of the mixed-wet sample captured from the drainage cycle during the two-phase flow coreflooding experiment.

2.2. Data Preprocessing

For both water-wet and mixed-wet samples, during the coreflooding experiment, the sample once loaded in the coreholder was never unloaded / moved till after the end of all intended cycles.

However, on examination of the reconstructed images, it could be seen that there were slight shifts in the global axis within the different fast batch scans. Additionally, angular misalignment was also noticed between the fast batch scans and the reference dry scan at the initial state of the sample. This meant that image registration had to be done. Considering the total number of datasets available, for computational efficiency, two functions namely shift, and rotate from SciPy [29] - the numerical library for Python programming was used. The initial slow scan of the water-wet / mixed-wet sample before the start of the experiment served as the reference datasets for the calculation of the image translation and rotation parameters of the numerous fast batch scans. The translated and rotated datasets were subsequently verified using the image registration module in Avizo™ ensuring that all datasets are well aligned.

2.3. U-ResNet Model Architecture

The U-ResNet model is a combination of a U-Net [31] and a ResNet [32] thereby taking advantage of the strengths of both these networks. The proficiency of a U-ResNet model for image segmentation in geosciences has been demonstrated in several publications [28, 33]. The architecture of the U-ResNet model used in our study was adapted from that published by Tang et al. [34]. The ability of their model to successfully perform multiphase segmentation on fuel cells was used as a benchmark for our dataset. However we optimized our model and tuned the hyperparameters to cater to the fast batch scans dataset and so the final model implemented has several differences to that used by Tang et al. [34]. The model optimization and tuning of parameters has been discussed in the results section of this paper.

The U-ResNet model was initially untrained and consists of 3 encoder blocks and 3 decoder blocks as shown in Figure 3. The encoder block is responsible for extracting key features of the image as well as reduce its spatial dimensions. This is made possible with the help of 2D convolutional blocks, batch normalization [35] which normalizes the training batches, an activation function namely rectified linear unit (ReLU) [36] and a MaxPool [37] block. Similarly, the restoration of the spatial dimensions of the image and the retention of features for segmentation is performed by the three decoder blocks. This is made possible with the help of 2D convolutional

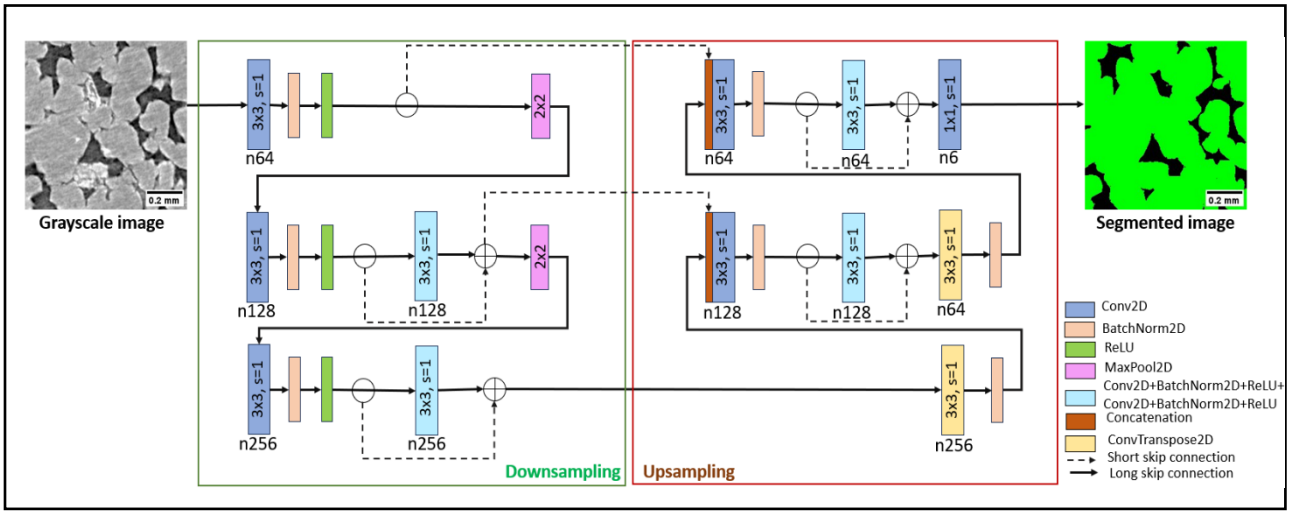

Fig. 3. Architecture of the U-ResNet model which consists of 3 encoder blocks that captures key features from the input image, while 3 decoder blocks retain this information during upsampling. The model also consists of short skip connections and long skip connection thereby preserving vital information.

transpose blocks and batch normalization. However, the key aspect of a U-ResNet [31, 32] model that enables it to perform better in comparison to other models for image segmentation is the inclusion of both short skip connections and long skip connections. The long skip connections connect the encoder to the decoder, thereby transferring features and information from the shallow convolution layers to the deeper layers. This helps in preserving high resolution information that would be otherwise lost during the downsampling process. The short skip connections on the other hand ensures that the model remains stable and solves the problem of vanishing gradients during back propagation. The final layer maps the features to the number of segmentation classes / labels as defined by the user.

To penalize the model during the training stage, cross-entropy loss function was included. The loss function determines how well the model can predict the labels in comparison to the provided ground truth dataset. Decreasing loss values for both the training and the testing dataset over the course of the model's training cycle indicates the improvement in the model's predicting capabilities. Cross-entropy loss is given by

$$Cross\ Entropy\ loss = -\sum_{i=1}^{N}\left(x_i log(y_i)\right) \quad (1)$$

where, N is total number of phases, x_i is the true probability of the ith phase, and y_i is the predicted probability of the ith phase.

2.4. Ground truth for Training Dataset

For the U-ResNet model to be effectively trained to perform two-phase segmentation, it was important to establish a ground truth segmentation for the chosen 2D training orthoslices. A common method for this could be the use of intensity thresholding and the Magic Wand feature from Avizo™ as demonstrated by Tang et al. [34], but around 80 orthoslices were chosen for training and so applying this workflow would be a laborious task. Furthermore, as mentioned earlier, traditional segmentation techniques require a degree of user judgement which leads to subsequent bias in fine tuning the segmented image. This is where machine learning techniques like WEKA segmentation is useful. Trainable Weka Segmentation (TWS) [38, 39] is an open-source software that is available as a plugin in the popular image processing toolkit Fiji [40]. In TWS, the input gray-scale image is treated as a pixel classification problem. A set of pixels belonging to the decane phase was labelled as decane and another set as grain + brine phase. These patches were used to train a random forest classifier, and it was then applied to the rest of the image. The selection of patches for training the WEKA segmentation classifier was done by an expert user, but the accuracy is still subjective as there still could be user-bias. The discrepancies arising from user-bias was not a concern as this would be reduced through both morphological analysis as well as during the inference stage by the trained and tested U-ResNet model. In this manner high-quality WEKA segmented 2D slices were generated and was selected as the ground truth data for training the model. However, it is noteworthy to mention that while WEKA is good at classifying 2D slices, it can struggle with 3D datasets depending on the domain size. While it took 9mins to segment a fast batch scan of 1536 x 1536 x 160 voxels, the algorithm failed to converge for larger domain sizes. Figure 4 shows an example of the WEKA segmented ground truth for the corresponding 2D gray-scale image of slice number 120 from fast batch scan 30 of the water-wet sample.

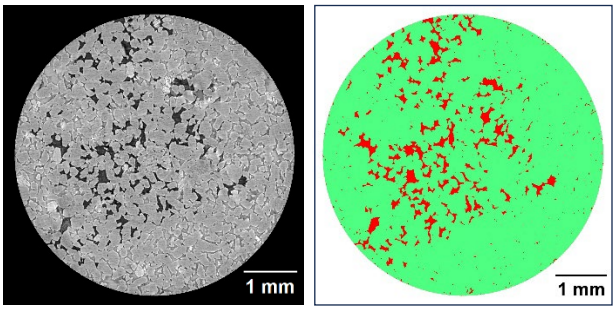

(a) (b)

Fig. 4. (a) Gray-scale image of slice number 120 from fast batch scan number 30 of drainage cycle 1 of the water-wet sample and (b) corresponding WEKA segmented 2D slice.

2.5. Model Training and Testing

The U-ResNet model was trained separately for the water-wet and mixed-wet sample mainly due to the significant presence of streak artifacts in the latter. Around 30 2D orthoslices of 1536 x 1536 pixels of varying nonwetting phase distributions were identified from different 3D datasets of the water-wet sample, and around 50 2D orthoslices were identified from the mixed-wet sample for the model's training. The slices were selected based on maximizing the features present across the dataset which not only included different saturation levels but also streak artifacts and minor beam hardening. These slices were cropped into 25000 patches of 256 x 256 pixels for training and 7000 patches for testing. The model was trained for 140 epochs with a batch size of 16 and learning rate of 0.00001 using AdamW solver [41]. A cosine annealing learning rate scheduler was included to adjust the learning rate based on a cosine function [42], which ensured that the learning rate dropped smoothly preventing any abrupt convergence of the model. This model was trained on a workstation with a single NVIDIA RTX 4090, 24 GB memory graphics card. The total training time for the water-wet sample was 13.3 hrs and that of the mixed-wet sample was 18.1 hrs with the available resources. The final trained and tested model required only 40s for the segmentation of a 3D fast batch dataset of 1536 x 1536 x 160 voxels.

2.6. Image Analysis

Prior to the assessment of the accuracy of the segmented images obtained from the trained and tested U-ResNet model, several steps of image processing were put in place to ensure accurate calculations. We implemented geodesic transformations [43] on all the binary segmented

images to ensure that isolated voxels were removed. Geodesic transformations involve the use of two input images, a marker image wherein the binary segmented image has undergone a morphological operation, and a mask image which is the original segmented image [44]. For our dataset, we performed significant erosion on the segmented image using a structuring element of cube of large radius, and this eroded image acted as the marker image. The geodesic transformation was performed using the reconstruction from markers module available in Avizo™. During the transformation, successive dilations are performed on the markers, and it ensures that a dilated marker will not merge into a particle other than the marks. In this manner, geodesic transformations are iterated till it reaches stability [44]. The advantage of this workflow is that when an eroded set is used as markers, it can rebuild the original shapes of the retained particles and only remove the isolated voxels. The transformations were applied to both the foreground and background of the dataset to get the final transformed image. It was also ensured that the interpretation was performed in 3D with a neighbourhood connectivity of 26. An example of the removal of isolated voxels using geodesic transformation from fast batch scan 30 of the water-wet sample is shown in Figure 5.

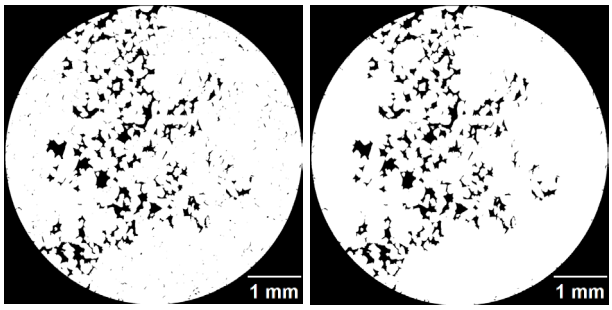

(a) (b)

Fig. 5. Fast batch scan number 30, slice 80 from drainage cycle 1 of the water-wet sample (a) before geodesic transformation shows isolated voxels (b) while after geodesic transformation, a lot of these regions are removed / minimized.

Since the fast batch scans resulted in partially saturated images, we used the technique explained by Culligan et al. [45] and Wildenschild et al. [18] to get ternary images. A dry reference scan was segmented by the U-ResNet model into a binary dataset with pores and grains. In the partially saturated images, the dataset was segmented into decane occupying pores as one phase and grains + brine as the 2nd phase. These two datasets are registered and then subtracted from each other to get a dataset which contains only the brine phase. The summation of the segmented dry scan along with this extracted brine phase dataset will result in a ternary image where the decane, brine and grain phases are clearly distinct. To prevent the external region or the region appearing outside the applied mask from interfering in the ternary image calculations, it was assigned a label of -1.

The commonly occurring partial volume effect [18] was observed in the three phase images and so necessary corrections needed to be done before any morphological analysis. The correction involved the dilation of the boundary phase using a pixel value of 2-5 across all datasets. Since the dry scan was used to generate the ternary images, it was used as the boundary reference phase. This helped to keep in check that the dilation process did not shift any boundaries. A region of interest (ROI) extracted from slice 0 of fast batch scan 19 of the mixed-wet sample is shown in Figure 6 to highlight the prominence of partial volume effect at the boundaries as visible in (b) while (c) shows the effect being corrected at the boundaries.

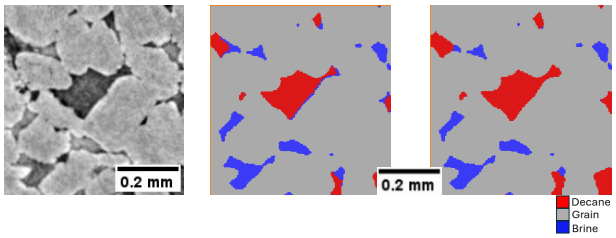

(a) (b) (c)

Fig. 6. Region of interest (ROI) taken from mixed-wet sample (a) fast batch scan number 19 from drainage cycle 1 to highlight the presence of (b) partial volume effect at the phase boundaries and (b) this effect being corrected using dilation.

2.6. Measurement of Segmentation Accuracy

Pixelwise accuracy and region-based accuracy measurements was implemented to verify the accuracy of the U-ResNet segmented images. At the end of each epoch of the training cycle, the mean Intersection-Over-Union (mIoU) was calculated for the testing batch dataset. This is a commonly used performance metric to evaluate image segmentation models by calculating the ratio of overlap between the predicted labels and the ground truth labels for an input gray-scale image [46, 47]. It is given by the equation,

$$mIoU = \frac{1}{N+1}\sum_{i=0}^{N}\frac{p_{ii}}{\sum_{j=0}^{N}p_{ij}+\sum_{j=0}^{N}p_{ji}-p_{ii}} \quad (2)$$

where $N+1$ represents the total number of phases, p_{ii} is the correctly predicted pixels belonging to phase i / true positives, p_{ij} is the number of pixels belonging to phase j but are predicted as phase i / false negatives, and p_{ji} is the number of pixels that belong to phase i but are predicted as phase j / false positives [34].

Another metric that was used to assess the segmentation results was the phase accuracy. It is the ratio between the number of true positives and the overall pixels (sum of true positives and false positives). This phase accuracy was calculated for the U-ResNet segmented binary images during the inference stage and is given by

$$Phase\ accuracy = \frac{p_{ii}}{p_{ii}+p_{ji}} \quad (3)$$

To calculate these metrics during inference, ground truth dataset is required, and so few slices from the water-wet sample and from the mixed-wet sample that was not used for training the U-ResNet model was selected. These

slices were carefully segmented by WEKA segmentation and kept aside as ground truth data.

2.7. Comparison of U-ResNet segmentation with Watershed Segmentation

An effective segmentation technique that is commonly used for multiphase segmentation is the watershed segmentation [20]. To compare the accuracy of our U-ResNet model with traditional methods like watershed segmentation, one of the fast batch scans from the mixed-wet sample was selected. The 3D domain was first filtered using non-local means filter and then was segmented using the watershed-based method available in Avizo™. Then a 2D slice from the mixed-wet sample containing streak artifacts was selected for comparison. On this 2D slice, the total phase accuracy, and mean Intersection-Over-Union (mIoU) was measured and visualized for each phase, and compared between the watershed segmented slice, the WEKA segmented (ground truth) image, and the U-ResNet segmented image. Finally, a 2D morphological analysis was also conducted using the imMinkowski package. The standard parameters such as perimeter, area, and 2D Euler characteristic of the labelled nonwetting phase, were computed and compared across the different segmented images. While the area is calculated by counting the intersection with 2D lines using the Crofton formula, the 2D Euler characteristic is calculated based on the number of connected components minus the number of holes [48].

3 Results and Discussion

In this section, we will first discuss the optimization of the U-ResNet architecture along with the tuning of hyperparameters. Following this, the training and testing cross-entropy losses along with the testing dataset segmentation accuracy results are showcased. Then inference conducted on one of the fast batch scans from both water-wet and mixed-wet sample is shown as examples of the model's performance. This includes phase accuracy calculations as well as visually inspecting regions where streak artifacts are prevalent. Additionally, a time-lapse of consecutive fast batch scans in both samples was visualized to observe pore-filling events. Finally, the segmentation of a selected dataset by our U-ResNet model is compared with watershed-based segmentation using the same metrics as mentioned earlier.

3.1. Optimization of the U-ResNet model

The U-ResNet model architecture that we initially deployed for our study had an additional encoder and decoder block resulting in a deeper model. Additionally, activation function, rectified linear unit (ReLU) was only enabled in the first encoder block. Some of the other key standouts was that the solver used was Adam [51] and a learning rate of 0.001 was initially set which was scheduled to reduce dynamically by 0.5 whenever the losses plateaued for 10 epochs. This model was scheduled to train for 140 epochs but during the monitoring of the test loss values, a classic case of overfitting was noticed from around 25 epochs as seen in the training versus testing cross-entropy loss plot in Figure 7. Anticipating that the model could stabilize, the model was allowed to continue its run but eventually the training was aborted after 70 epochs. The upward trend of the testing data's cross-entropy loss plot showed us that the model was not learning anything, but rather memorizing patterns in the training data. This implied that either the training dataset was not diverse enough or that the model's architecture was too complex.

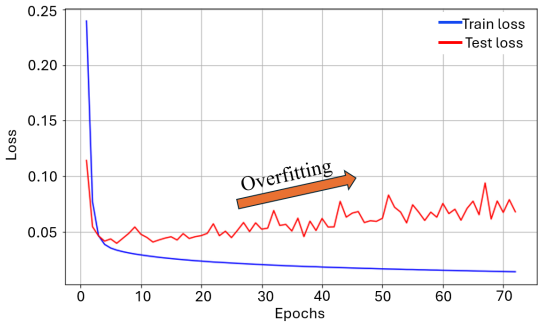

Fig. 7. Training versus testing cross-entropy loss plot for the mixed-wet sample with a deeper U-ResNet model comprising of 4 encoder and 4 decoder blocks. Testing loss values demonstrate a classic case of overfitting.

After several iterations, it occurred to us that the model was too complex for our dataset and so the architecture was modified to only 3 encoder and 3 decoder blocks. Additionally, the solver was switched to AdamW and a cosine function was put in place to control the learning rate. These modifications in the model's architecture and the hyperparameters helped in stabilizing the model. This exercise also sheds light on the fact that deeper and complex neural networks does not necessarily mean better results especially in applications like image segmentation. Depending on the complexity of the training dataset, and the task in hand, it is advisable to be cautious when choosing the right model and architecture. As seen here, deeper models can lead to overfitting and no new information is being added by the extra layers. The final architecture for our U-ResNet model is as described in Section 2.1.

3.1. Accuracy of Testing Dataset Results

The training versus testing cross-entropy loss plot for the mixed-wet sample is shown in Figure 8. The plot shows that the cross-entropy loss for the testing dataset converged to a value of 0.04 and showed stability till the end of the training cycle of 140 epochs. Correspondingly the testing accuracy was recorded to have converged to 0.98 at the end of the run, where a value of 1.0 is the maximum accuracy. On the other hand, the mean Intersection-Over-Union (mIoU) for the testing dataset converged to a value of 0.93 indicating a high level of accuracy between the predicted labels and the ground truth labels. Though the training versus testing cross-

entropy loss plot for only the mixed-wet sample is shown, similar values were recorded for the water-wet sample as well. The cross-entropy loss for the testing dataset converged to a value of 0.03 while testing accuracy was 0.98 and the mean Intersection-Over-Union (mIoU) was recorded as 0.95.

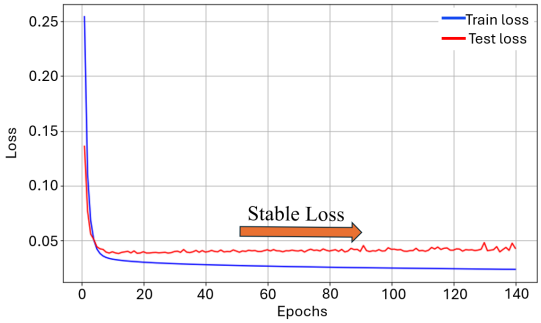

Fig. 8. Training versus testing cross-entropy loss plot for the mixed-wet sample with U-ResNet model as a function of epochs.

The label prediction / segmentation results by the U-ResNet model during the testing stage of the water-wet sample as recorded at 121 epochs is depicted in Figure 9. The figure shows the input gray-scale image along with the WEKA segmented image that is fed as ground truth and finally the prediction by the U-ResNet model. Visual confirmation indicates that the predicted labels closely match that of the ground truth labels

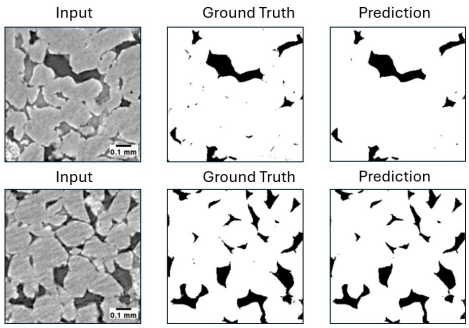

Fig. 9. Input gray-scale image, WEKA segmented ground truth segmented image, and finally the U-ResNet predicted segmented image of the testing dataset of the water-wet sample.

3.2. Accuracy of Inference Dataset Results

Since the results of the testing dataset showed good accuracy, the model was then deployed on unseen data, which includes all the slices from the fast batch scans that was not used for training and testing the network. The phase accuracy of the two-phase segmented images by the trained and tested U-ResNet model is visualized in the form of a confusion matrix as depicted in Figure 10. The accuracy of several slices was calculated, but as an example 1 slice each from the water-wet, and mixed-wet sample is shown here. In the figure, the confusion matrices are of (a) slice 100 from fast batch scan 30 of the water-wet sample, and (b) slice 80 from fast batch scan 21 from the mixed-wet sample. The confusion matrices demonstrate that in both cases, the grain + brine phase is accurately labelled by the U-ResNet model, followed by the decane phase which itself shows a high accuracy varying from 0.93 to 0.94, where 1.0 is the maximum accuracy.

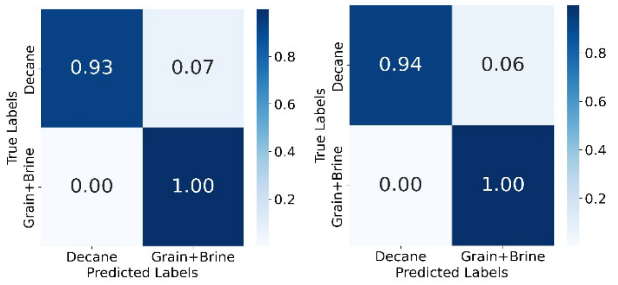

Fig. 10. Confusion matrix the U-ResNet segmentation results of (a) Slice 100 of fast batch scan number 30 (water-wet) (b) Slice 80 of fast batch scan number 21 (mixed-wet). Both matrices show a good accuracy for decane phase prediction.

Since streak artifacts were prominent across the datasets, a visual inspection was done of the datasets to assess the performance of the U-ResNet in mitigating these artifacts. Regions of interest (ROI) from the decane flooded mixed-wet sample prior to the drainage cycle as well as ROI from the fast batch dataset was selected for this purpose. The streak artifacts in the water-wet sample were not as prominent and so is not discussed here. These selected slices were not used in the training of the U-ResNet model. In Figure 11, (a) and (b) which are slices 807 and 756 from the dry sample, it can be seen in the segmentation results that the U-ResNet model has accurately classified the regions covered by the streak artifacts. These regions otherwise would have been misclassified as pore in the grain regions and affected further physical calculations.

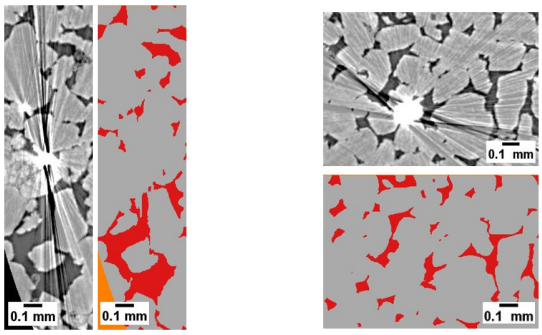

Fig. 11. Regions of interest (ROI) of prominent streak artifacts depicted as gray-scale images and their corresponding U-ResNet segmentation – (a) Slice number 807, and (b) slice number 756 from the dry mixed-wet sample.

To further verify the segmentation accuracies, mean Intersection-Over-Union (mIoU) was calculated for slice 100 and slice 80 of water-wet and mixed-wet samples respectively, and the score was an average of 0.96. This meant that 96% of the U-ResNet segmented image overlaps well over the WEKA segmented image. It is noteworthy to mention that since the ground truth datasets were manually segmented with the help of WEKA segmentation, it is possible that errors / bias could have occurred in these regions in the training dataset. While

this inherent bias is unavoidable, the trained U-ResNet would be consistent across all data sets. Overall, the accuracy measures of both mIoU and the phase accuracy indicate that the segmentation results by the U-ResNet model are quite accurate. Additionally, visual inspection of regions with streak artifacts also confirm that the U-ResNet model has prevented any mislabelling of pixels.

3.3. Time-Lapse of Decane invading Pore Spaces

Figure 12 depicts two consecutive fast batch scans (a) 30 and (b) 31 of the water-wet sample after applying U-ResNet segmentation and the image processing workflow explained in Section 2.6. These fast batch scans were selected to observe the invasion of decane which is mostly prominent from scans 30 to 49 with a major flooding evident occurring between adjacent scans 30 and 31.

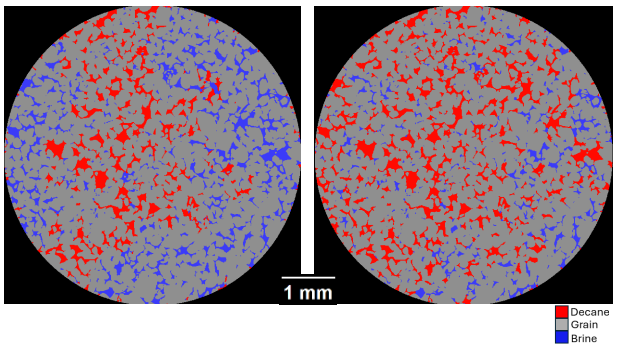

(a) (b)

Fig. 12. A sequence of percolation of decane in the pore spaces as captured during the fast batch scans (a) 30 and (b) 31 of the water-wet sample.

For a closer look at the flow of decane into the water-wet sample, 3 consecutive fast batch scans 30, 31, and 32 were visualized as a time-lapse event in the XZ direction which is the direction of flow. This time-lapse event is depicted as 3D renderings in Figure 13. Several pore filling events can be seen across the consecutive fast batch scans, and as expected during a drainage cycle in the water-wet sample, the decane fills the larger pores and throats first.

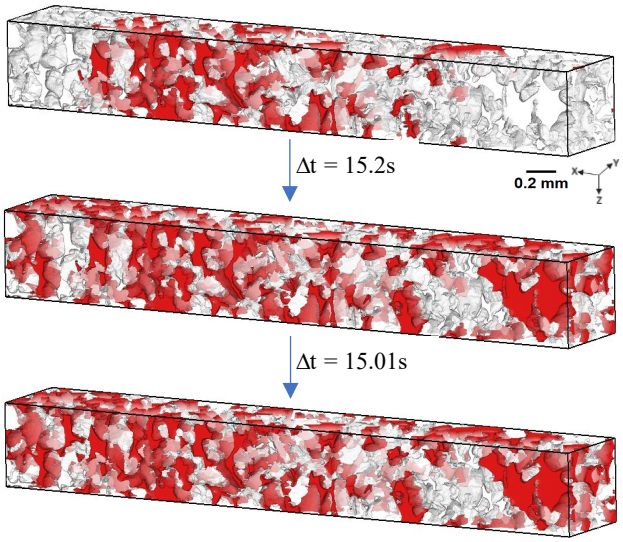

Fig. 13. Time-lapse of decane pushing out brine from the pore spaces in the water-wet sample as visualized in the direction of flow, XZ direction. Only pore spaces are depicted in this 3D rendering and not the solid matrix, decane is shown in red.

Figure 14 depicts two consecutive fast batch scans (a) 18 and (b) 19 of the mixed-wet sample. These fast batch scans indicate that decane has pushed out brine in a much faster rate (fast batch scan 18) in comparison to the water-wet sample (fast batch scan 30) though the flow rate was consistent across both samples with the same pore volumes injected per scan. This could be due to the presence of partial oil-wet pores in the mixed-wet sample facilitating more disperse invasion of decane.

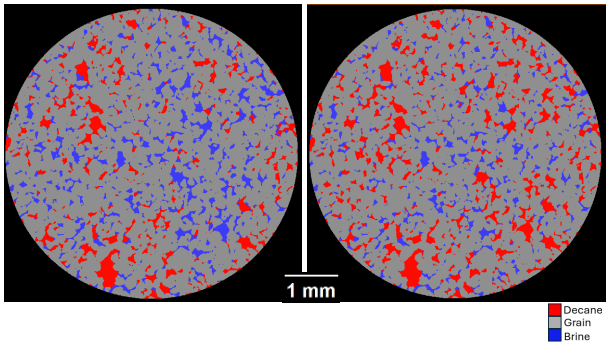

(a) (b)

Fig. 14. A sequence of percolation of decane in the pore spaces as captured during the fast batch scans (a) 18 (b) 19 of the mixed-wet sample.

The time-lapse event of percolation of decane in the mixed-wet sample across fast batch scans 18, 19, and 20 is shown in Figure 15. As observed, the oil tends to occupy large and small pores in approximately equal proportion, suggesting that mixed-wet conditions were achieved.

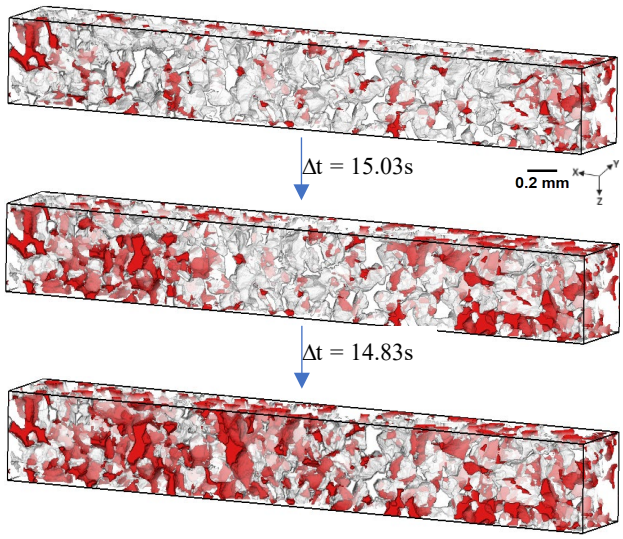

Fig. 15. Time-lapse of decane pushing out brine from the pore spaces in the mixed-wet sample as visualized in the direction of flow, XZ direction. Only pore spaces are depicted in this 3D rendering and not the solid matrix, decane is shown in red.

Although these visualizations further substantiate the accuracy of our U-ResNet model, a thorough morphological analysis is necessary to study the pore-

scale physics. At this point, we can only make qualitative assessments that demonstrate the resulting images are free or artifacts, capture pore filling events, and demonstrate consistently different behaviors between the water-wet and mixed-wet samples.

3.4. Comparison of U-ResNet segmentation results with Watershed segmentation

To compare the segmentation accuracy of our U-ResNet model with watershed-based segmentation, batch scan 19 of the mixed-wet sample was selected. In Avizo™, the non-local means filter was applied before conducting watershed segmentation. The non-local means filter was recorded to have taken 40s for denoising the selected fast batch scan of domain size 1536 x 1536 x 160 voxels. The watershed segmentation took 1min20s to segment this dataset. Therefore, the workflow to apply watershed segmentation took 2mins to segment a 3D dataset of this domain size, while our U-ResNet model required 40s for the same 3D dataset. Table 1 shows a comparison of the time taken by watershed segmentation and our U-ResNet model to segment all 50 fast batch scans of the drainage cycle of each sample. The total time required to segment the fast batch scans demonstrates that our U-ResNet model is 3 times faster, 67% more efficient than the watershed segmentation. It is noteworthy to mention that this time recorded by the U-ResNet model was the processing time using a single NVIDIA GPU of 24 GB memory. This performance can be enhanced by using multiple GPUs as the 3D datasets can be processed in parallel, thereby reducing the segmentation time even further.

Table 1. Comparison of time taken to segment 50 fast batch scans of 3D domain size 1536 x 1536 x 160 by watershed segmentation and our U-ResNet model.

	Domain size (voxels)	Segmentation Time	Drainage Cycle – Domain size (voxels)	Total Segmentation Time	Improved Efficiency
Non-local means filter + Watershed Segmentation	1536 x 1536 x 160	2mins	(1536 x 1536 x 160) * 50	1hr40mins	
U-ResNet	1536 x 1536 x 160	40s	(1536 x 1536 x 160) * 50	33mins	67%

For visual comparison, slice 82 of fast batch scan 19 was selected as this slice consists of streak artifacts. Figure 16 (a) depicts region of interest (ROI) of the streak artifact which is segmented by (b) by watershed segmentation and (c) our U-ResNet model for comparison. In these binary segmented images where decane is classified as one phase, and grain + brine is classified as another phase, streaks are clearly misclassified as decane in the watershed segmented ROI as evident in sub-figure (b). This implies that further image processing and analysis would be affected by these misclassified regions. On the other hand, our U-ResNet model has nullified the effect of streak artifacts as seen in sub-figure (c), thus highlighting the accuracy of this model in mitigating such effects.

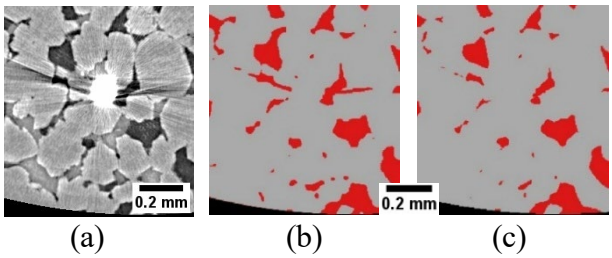

Fig. 16. Visual comparison of streak artifact mitigation. (a) Slice 82, fast batch scan 19, mixed-wet sample region of interest (ROI). (b) Watershed segmentation ROI (d) U-ResNet segmentation ROI. U-ResNet model has reduced the effects of streak artifacts successfully.

To compare the segmentation accuracy, the phase accuracy of the same selected 2D slice number 82 was calculated and was found to be 99.12% for the U-ResNet model, and 97.38% for the watershed segmented image. For further investigation of the segmentation accuracy, mean Intersection-Over-Union (mIoU) was calculated and the mIoU score was found to be 95.9% for our U-ResNet model and 90.2% for watershed segmentation. This means that for our U-ResNet model, nearly 96% of the predicted segmented image overlaps well with the WEKA segmented / ground truth image. A lower mIoU score for watershed segmentation in comparison to phase accuracy is because mIoU penalizes boundary mismatches, and thus misclassified regions like streak artifacts will affect its score while phase accuracy only counts the number of correctly labelled pixels without considering boundaries. The mIoU score was then visualized for the decane phase and grain + brine phase in the form of bar graphs as shown in Figure 17. The figure shows that our U-ResNet model outperforms the watershed segmentation in labelling each phase.

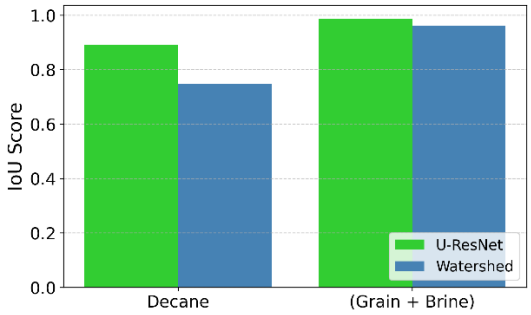

Fig. 17. Mean Intersection-Over-Union (mIoU) visualized for both decane and (grain + brine) phase to compare U-ResNet segmentation with watershed segmentation. The bar graphs indicate U-ResNet outperforms watershed segmentation.

Table 2 shows a comparison of the percentage error differences in computations of the 2D Minkowski functionals, i.e., area, perimeter, and 2D Euler characteristic of the nonwetting phase across both U-ResNet and watershed segmented 2D slice in comparison to the WEKA segmented / ground truth 2D slice number 82 of fast batch scan 19. Table 2 shows that while area and perimeter have -7% and -2% percent error difference between the U-ResNet segmented image and the WEKA segmented image, the percentage error difference is 28%

and 47% for the watershed segmented image. Additionally, 2D Euler characteristic for the U-ResNet image indicates only a 2% error when compared to the ground truth image, while the watershed segmentation shows a high percentage error difference of 166%. Thus, the table highlights that U-ResNet segmented image has the least percentage errors in the 2D Minkowski functionals when compared to the WEKA segmented image.

Table 2. Comparison of 2D Minkowski functionals of WEKA segmented image / ground truth, Watershed segmentation, U-ResNet segmented image.

	Area (μm^2)	Error	Perimeter (μm)	Error	Euler2D	Error
WEKA (Ground Truth)	$1.87x10^5$		$4.06x10^4$		874	
Watershed Segmentation	$2.39x10^5$	28%	$5.96x10^4$	47%	2323	166%
U-ResNet	$1.73x10^5$	-7%	$3.99x10^4$	-2%	892	2%

4 Conclusion

A U-ResNet model was presented that can segment fast batch scans of porous media captured at 1s with 15-16s time lapse intervals during multiphase drainage coreflooding experiment conducted on synchrotron based micro-CT systems with focussed mitigation of streak artifacts. 30 to 50 2D orthoslices that included slices with strong streak artifacts were segmented using WEKA segmentation and used for training the model. The model was trained separately for the water-wet sample, and the mixed-wet sample, and on testing, it was seen that while the testing accuracy was 0.98 for both samples, the mean intersection over union varied between 0.93 and 0.95 which can act as an indicator that the U-ResNet predicted segmentation was mitigating the effects of streak artifacts. This was later verified visually in the inference datasets. Furthermore, phase accuracies visualized in the form of confusion matrices on the inference dataset showed a range of 0.93 to 0.94.

Additionally, our U-ResNet model was compared with traditional methods like watershed segmentation on a 2D slice from the mixed-wet sample that had prominent streak artifacts. It was seen that our U-ResNet model outperformed watershed segmentation in mitigating these streak artifacts which was observed both visually and as well as the total mIoU score and phase mIoU score wherein the U-ResNet model provided a higher score. The performance of our U-ResNet model was further assessed by conducting a 2D morphological analysis and compared with that of watershed segmentation. It was seen that our U-ResNet model could capture 2D Minkowski functionals at an average of -2% error.

The significant strength of our U-ResNet model lies in the fact that it requires only 1/3rd of the time to segment a 3D domain size of 1536 x 1536 x 160 voxels when compared to watershed segmentation. This means that for a drainage cycle of 50 batch scans, our U-ResNet model is 3 times faster or 67% more efficient on a single NVIDIA GPU of 24GB memory. The implications of this are that with multiplied GPUs, parallel processing becomes possible thereby reducing the time required to accurately segment large datasets even further. Overall, this analysis indicates that the U-ResNet model performs better than traditional methods like watershed segmentation not only in terms of speed but also in accuracy as confirmed by both visual and metric calculations.

References:

1. Bultreys, T., M.A. Boone, M.N. Boone, T. De Schryver, B. Masschaele, D. Van Loo, L. Van Hoorebeke, and V. Cnudde, *Real-time visualization of Haines jumps in sandstone with laboratory-based microcomputed tomography.* Water Resour. Res., **51**(10): p. 8668-8676, (2015).
2. Held, R.J. and M.A. Celia, *Pore-scale modeling and upscaling of nonaqueous phase liquid mass transfer.* Water Resour. Res., **37**: p. 539-549, (2001).
3. Zuo, L. and S.M. Benson, *Process-dependent residual trapping of CO2 in sandstone.* Geophys. Res. Lett., **41**(8): p. 2820-2826, (2014).
4. Boerckel, J.D., D.E. Mason, A.M. McDermott, and E. Alsberg, *Microcomputed tomography: approaches and applications in bioengineering.* **5**(6): p. 144, (2014).
5. Wildenschild, D. and A.P. Sheppard, *X-ray imaging and analysis techniques for quantifying pore-scale structure and processes in subsurface porous medium systems.* Adv. Water Resour., **51**: p. 217-246, (2013).
6. Armstrong, R.T., H. Ott, A. Georgiadis, M. Rücker, A. Schwing, and S. Berg, *Subsecond pore-scale displacement processes and relaxation dynamics in multiphase flow.* Water Resour. Res., **50**(12): p. 9162-9176, (2014).
7. Berg, S., H. Ott, S.A. Klapp, A. Schwing, R. Neiteler, N. Brussee, A. Makurat, L. Leu, F. Enzmann, J.-O. Schwarz, M. Kersten, S. Irvine, and M. Stampanoni, *Real-time 3D imaging of Haines jumps in porous media flow.* **110**(10): p. 3755-3759, (2013).
8. Berg, S., R. Armstrong, H. Ott, A. Georgiadis, S.A. Klapp, A. Schwing, R. Neiteler, N. Brussee, A. Makurat, L. Leu, F. Enzmann, J.-O. Schwarz, M. Wolf, F. Khan, M. Kersten, S. Irvine, and M. Stampanoni, *Multiphase Flow in Porous Rock Imaged Under Dynamic Flow Conditions with Fast X-Ray Computed Microtomography.* Petrophysics **55**(04): p. 304-312, (2014).
9. Meisenheimer, D.E., M.L. Rivers, and D. Wildenschild, *Optimizing pink-beam fast X-ray microtomography for multiphase flow in 3D porous media.* J. Microsc., **277**(2): p. 100-106, (2020).
10. Haines, W.B., *Studies in the physical properties of soil. V. The hysteresis effect in capillary properties, and the modes of moisture*

distribution associated therewith. J. Agric. Sci., **20**(1): p. 97-116, (1930).
11. Roof, J.G., *Snap-Off of Oil Droplets in Water-Wet Pores.* Soc. Pet. Eng. J., **10**(01): p. 85-90, (1970).
12. Youssef, S., H. Deschamps, J. Dautriat, E. Rosenberg, R. Oughanem, E. Maire, and R. Mokso. *4D imaging of fluid flow dynamics in natural porous media with ultra-fast X-ray microtomography*. in *International Symposium of Core Analyst*. Napa Valley, California, USA,(2013).
13. Leu, L., S. Berg, F. Enzmann, R.T. Armstrong, and M. Kersten, *Fast X-ray Micro-Tomography of Multiphase Flow in Berea Sandstone: A Sensitivity Study on Image Processing.* Transp. Porous Media., **105**(2): p. 451-469, (2014).
14. Rücker, M., S. Berg, R. Armstrong, A. Georgiadis, H. Ott, L. Simon, F. Enzmann, M. Kersten, and S. de With. *The fate of oil clusters during fractional flow: trajectories in the saturation-capillary number space*. in *Internationl Symposium of the Society of Core Analysts*. St. John's, Newfoundland and Labrador, Canada,(2015).
15. Bultreys, T., K. Singh, A.Q. Raeini, L.C. Ruspini, P.-E. Øren, S. Berg, M. Rücker, B. Bijeljic, and M.J. Blunt, *Verifying Pore Network Models of Imbibition in Rocks Using Time-Resolved Synchrotron Imaging.* Water Resour. Res., **56**(6): p. e2019WR026587, (2020).
16. Bultreys, T., S. Ellman, C.M. Schlepütz, M.N. Boone, G.K. Pakkaner, S. Wang, M. Borji, S. Van Offenwert, N. Moazami Goudarzi, W. Goethals, C.W. Winardhi, and V. Cnudde, *4D microvelocimetry reveals multiphase flow field perturbations in porous media.* **121**(12): p. e2316723121, (2024).
17. Singh, K., H. Menke, M. Andrew, Q. Lin, C. Rau, M.J. Blunt, and B. Bijeljic, *Dynamics of snap-off and pore-filling events during two-phase fluid flow in permeable media.* **7**(1): p. 5192, (2017).
18. Wildenschild, D., M.L. Rivers, M.L. Porter, G.C. Iltis, R.T. Armstrong, and Y. Davit, *Using Synchrotron-Based X-Ray Microtomography and Functional Contrast Agents in Environmental Applications*, in *Soil–Water–Root Processes: Advances in Tomography and Imaging*. p. 1-22,(2013).
19. Otsu, N., *A Threshold Selection Method from Gray-Level Histograms.* **9**(1): p. 62-66, (1979).
20. Meyer, F. and S. Beucher, *Morphological segmentation*. J. Vis. Commun. Image Represent., **1**(1): p. 21-46, (1990).
21. Phan, J., L.C. Ruspini, and F. Lindseth, *Automatic segmentation tool for 3D digital rocks by deep learning.* **11**(1): p. 19123, (2021).
22. Garfi, G., C.M. John, S. Berg, and S. Krevor, *The sensitivity of estimates of multiphase fluid and solid properties of porous rocks to image processing.* Transp. Porous Media., **131**(3): p. 985-1005, (2020).
23. Wang, Y.D., M.J. Blunt, R.T. Armstrong, and P. Mostaghimi, *Deep learning in pore scale imaging and modeling.* Earth Sci. Rev., **215**: p. 103555, (2021).
24. Hebert, V., T. Porcher, V. Planes, M. Léger, A. Alperovich, B. Goldluecke, O. Rodriguez, and S. Youssef, *Digital core repository coupled with machine learning as a tool to classify and assess petrophysical rock properties.* **146**: p. 01003, (2020).
25. Tang, K., Y. Da Wang, J. McClure, C. Chen, P. Mostaghimi, and R.T. Armstrong, *Generalizable Framework of Unpaired Domain Transfer and Deep Learning for the Processing of Real-Time Synchrotron-Based X-Ray Microcomputed Tomography Images of Complex Structures.* Phys. Rev. Appl., **17**(3): p. 034048, (2022).
26. Niu, Y., P. Mostaghimi, M. Shabaninejad, P. Swietojanski, and R.T. Armstrong, *Digital Rock Segmentation for Petrophysical Analysis With Reduced User Bias Using Convolutional Neural Networks.* Water Resour. Res., **56**(2): p. e2019WR026597, (2020).
27. Karimpouli, S. and P. Tahmasebi, *Segmentation of digital rock images using deep convolutional autoencoder networks.* Comput. Geosci., **126**: p. 142-150, (2019).
28. Wang, Y.D., M. Shabaninejad, R.T. Armstrong, and P. Mostaghimi, *Deep neural networks for improving physical accuracy of 2D and 3D multi-mineral segmentation of rock micro-CT images.* ASC, **104**: p. 107185, (2021).
29. Virtanen, P., R. Gommers, T.E. Oliphant, M. Haberland, T. Reddy, D. Cournapeau, E. Burovski, P. Peterson, W. Weckesser, J. Bright, S.J. van der Walt, M. Brett, J. Wilson, K.J. Millman, N. Mayorov, A.R.J. Nelson, E. Jones, R. Kern, E. Larson, C.J. Carey, İ. Polat, Y. Feng, E.W. Moore, J. VanderPlas, D. Laxalde, J. Perktold, R. Cimrman, I. Henriksen, E.A. Quintero, C.R. Harris, A.M. Archibald, A.H. Ribeiro, F. Pedregosa, P. van Mulbregt, A. Vijaykumar, A.P. Bardelli, A. Rothberg, A. Hilboll, A. Kloeckner, A. Scopatz, A. Lee, A. Rokem, C.N. Woods, C. Fulton, C. Masson, C. Häggström, C. Fitzgerald, D.A. Nicholson, D.R. Hagen, D.V. Pasechnik, E. Olivetti, E. Martin, E. Wieser, F. Silva, F. Lenders, F. Wilhelm, G. Young, G.A. Price, G.-L. Ingold, G.E. Allen, G.R. Lee, H. Audren, I. Probst, J.P. Dietrich, J. Silterra, J.T. Webber, J. Slavič, J. Nothman, J. Buchner, J. Kulick, J.L. Schönberger, J.V. de Miranda Cardoso, J. Reimer, J. Harrington, J.L.C. Rodríguez, J. Nunez-Iglesias, J. Kuczynski, K. Tritz, M. Thoma, M. Newville, M. Kümmerer, M. Bolingbroke, M. Tartre, M. Pak, N.J. Smith, N. Nowaczyk, N. Shebanov, O. Pavlyk, P.A. Brodtkorb, P. Lee, R.T. McGibbon, R. Feldbauer, S. Lewis, S. Tygier, S. Sievert, S. Vigna, S. Peterson, S. More, T. Pudlik, T.

Oshima, T.J. Pingel, T.P. Robitaille, T. Spura, T.R. Jones, T. Cera, T. Leslie, T. Zito, T. Krauss, U. Upadhyay, Y.O. Halchenko, Y. Vázquez-Baeza and C. SciPy, *SciPy 1.0: fundamental algorithms for scientific computing in Python*. **17**(3): p. 261-272, (2020).

30. Estienne, T., M. Vakalopoulou, S. Christodoulidis, E. Battistela, M. Lerousseau, A. Carre, G. Klausner, R. Sun, C. Robert, S. Mougiakakou, N. Paragios, and E. Deutsch. *U-ReSNet: Ultimate Coupling of Registration and Segmentation with Deep Nets*. in *Medical Image Computing and Computer Assisted Intervention – MICCAI 2019*. Cham: Springer International Publishing,(2019).
31. Ronneberger, O., P. Fischer, and T. Brox. *U-Net: Convolutional Networks for Biomedical Image Segmentation*. in *Medical Image Computing and Computer-Assisted Intervention – MICCAI 2015*. Cham: Springer International Publishing,(2015).
32. He, K., X. Zhang, S. Ren, and J. Sun. *Deep residual learning for image recognition*. in *Proceedings of the IEEE conference on computer vision and pattern recognition*.(2016).
33. Siavashi, J., M. Mahdaviara, M.J. Shojaei, M. Sharifi, and M.J. Blunt, *Segmentation of two-phase flow X-ray tomography images to determine contact angle using deep autoencoders.* **288**: p. 129698, (2024).
34. Tang, K., Q. Meyer, R. White, R.T. Armstrong, P. Mostaghimi, Y. Da Wang, S. Liu, C. Zhao, K. Regenauer-Lieb, and P.K.M. Tung, *Deep learning for full-feature X-ray microcomputed tomography segmentation of proton electron membrane fuel cells.* **161**: p. 107768, (2022).
35. Ioffe, S. and C. Szegedy, *Batch Normalization: Accelerating Deep Network Training by Reducing Internal Covariate Shift*, in *Proceedings of the 32nd International Conference on Machine Learning*, B. Francis and B. David, Editors. 2015, PMLR: Proceedings of Machine Learning Research. p. 448--456.
36. Agarap, A.F., *Deep Learning using Rectified Linear Units (ReLU).* (2018).
37. Scherer, D., A. Müller, and S. Behnke. *Evaluation of Pooling Operations in Convolutional Architectures for Object Recognition*. in *Artificial Neural Networks – ICANN 2010*. Berlin, Heidelberg: Springer Berlin Heidelberg,(2010).
38. Arganda-Carreras, I., V. Kaynig, C. Rueden, K.W. Eliceiri, J. Schindelin, A. Cardona, and H. Sebastian Seung, *Trainable Weka Segmentation: a machine learning tool for microscopy pixel classification.* **33**(15): p. 2424-2426, (2017).
39. Hall, M., E. Frank, G. Holmes, B. Pfahringer, P. Reutemann, and I.H. Witten, *The WEKA data mining software: an update.* **11**(1): p. 10–18, (2009).
40. Schindelin, J., I. Arganda-Carreras, E. Frise, V. Kaynig, M. Longair, T. Pietzsch, S. Preibisch, C. Rueden, S. Saalfeld, B. Schmid, J.-Y. Tinevez, D.J. White, V. Hartenstein, K. Eliceiri, P. Tomancak, and A. Cardona, *Fiji: an open-source platform for biological-image analysis.* **9**(7): p. 676-682, (2012).
41. Loshchilov, I. and F. Hutter. *Decoupled Weight Decay Regularization*. in *International Conference on Learning Representations*.(2017).
42. Paszke, A., S. Gross, F. Massa, A. Lerer, J. Bradbury, G. Chanan, T. Killeen, Z. Lin, N. Gimelshein, L. Antiga, A. Desmaison, A. Köpf, E. Yang, Z. DeVito, M. Raison, A. Tejani, S. Chilamkurthy, B. Steiner, L. Fang, J. Bai, and S. Chintala, *PyTorch: an imperative style, high-performance deep learning library*, in *Proceedings of the 33rd International Conference on Neural Information Processing Systems*, Curran Associates Inc. p. Article 721,(2019).
43. Lantuejoul, C. and F. Maisonneuve, *Geodesic methods in quantitative image analysis.* **17**(2): p. 177-187, (1984).
44. Soille, P., *Geodesic Transformations*, in *Morphological Image Analysis: Principles and Applications*, P. Soille, Editor, Springer Berlin Heidelberg: Berlin, Heidelberg. p. 183-218,(2004).
45. Culligan, K.A., D. Wildenschild, B.S.B. Christensen, W.G. Gray, M.L. Rivers, and A.F.B. Tompson, *Interfacial area measurements for unsaturated flow through a porous medium.* **40**(12), (2004).
46. Bihani, A., H. Daigle, J.E. Santos, C. Landry, M. Prodanović, and K. Milliken, *MudrockNet: Semantic segmentation of mudrock SEM images through deep learning.* **158**: p. 104952, (2022).
47. Rahman, M.A. and Y. Wang. *Optimizing Intersection-Over-Union in Deep Neural Networks for Image Segmentation*. in *Advances in Visual Computing*. Cham: Springer International Publishing,(2016).
48. Legland, D., K. KiÊN, and M.-F. Devaux, *Computation of Minkowski measures on 2D and 3D binary images.* **26**, (2007).
49. Legland, D., *imMinkowski - MATLAB Central File Exchange*. 2024.
50. Armstrong, R.T., J.E. McClure, V. Robins, Z. Liu, C.H. Arns, S. Schlüter, and S. Berg, *Porous Media Characterization Using Minkowski Functionals: Theories, Applications and Future Directions.* Transp. Porous Media., **130**(1): p. 305-335, (2019).
51. Kingma, D.P. and J. Ba, *Adam: A method for stochastic optimization*. (2014).